Exploring the Relationship between Deposition Method, Microstructure, and Performance of Nb/Si-based Superconducting Coplanar Waveguide Resonators

Jin-Su Oh[1], Cameron J. Kopas,[2] Jayss Marshall,[2] Xiaotian Fang,[1] Kamal R. Joshi,[1] Amlan Datta,[1,3] Sunil Ghimire,[1,3] Joong-Mok Park,[1] Richard Kim,[1] Daniel Setiawan,[2] Ella Lachman,[2] Joshua Y. Mutus,[2] Akshay A. Murthy,[4] Anna Grassellino,[4] Alex Romanenko,[4] John Zasadzinski,[5] Jigang Wang,[1,3] Ruslan Prozorov,[1,3] Kameshwar Yadavalli,[2] Matt Kramer,[1] and Lin Zhou[1,6*]

[1]Ames National Laboratory, Ames, Iowa 50011, United States

[2] Rigetti Computing, Berkeley, California 94710, United States

[3] Department of Physics & Astronomy, Iowa State University, Ames, Iowa 50011, United States

[4] Superconducting Quantum Materials and Systems Division, Fermi National Accelerator Laboratory, Batavia, Illinois 60510, United States

[5] Department of Physics, Illinois Institute of Technology, Chicago, Illinois 60616, United States

[6] Department of Materials Science and Engineering, Iowa State University, Ames, Iowa 50011, United States

*Corresponding author: linzhou@ameslab.gov

Abstract

Superconducting quantum circuits (SQC) are one of the most promising hardware platforms for quantum computing, yet their performance is currently limited by the presence of various structural defects inside the circuit's structure. Despite impressive progress in the past decade, a precise understanding of the origin of these defects from various fabrication processes and their impact on coherence is still lacking. In this study, we performed a comprehensive investigation on the microstructure, superconductivity, and resonator quality factor of Nb films deposited by high-power impulse magnetron sputtering (HiPIMS) and direct current (DC) magnetron sputtering. A suite of characterization techniques, including electron microscopy with spectroscopy, secondary ion mass spectrometry, magneto-optical microscopy, and pump-probe reflectivity spectroscopy is used. We reveal that niobium (Nb) resonators fabricated using HiPIMS exhibit a smaller average grain size, thicker surface oxide with larger thickness variations (rougher surface), and a thicker amorphous Nb/Si interface layer compared to samples deposited by DC sputtering. We identified that the amorphous Nb oxides (mainly located at the Nb surface and along the grain boundaries) and Nb-Si amorphous layers (at the Nb/Si interface) are major and potential sources of two-level system (TLS), while off-stochiometric oxides and suboxides of Nb close to the surface, crystalline defects (i.e., dislocations at grain boundary, point defects introduced during deposition) are main contributors of non-TLS sources. Our findings clarify the relationship between different defects and coherence loss mechanisms, highlighting the importance of material microstructure control on performance optimization in SQC.

1. Introduction

The emergence of quantum information processing (QIP) is a promising technology for potentially simulating quantum physics, chemistry, and optimization algorithms [1–6]. Among the hardware platforms for quantum computing, superconducting quantum bits (qubits) have emerged as a leading hardware architecture [7–11]. Despite significant progress in the fabrication and design of quantum circuits [12–14], superconducting qubits' performance, measured by parameters such as T_1 (relaxation time) and T_2 (decoherence time), is still far below theoretical estimations [9,15]. Therefore, it is crucial to gain a deeper understanding of the intrinsic materials' properties, both in- and out-of-superconducting states, and their impact on decoherence processes, as demonstrated by studies on the material-related decoherence sources in superconducting qubits, aiming to improve their performance and enable large-scale deployments [16–18].

Superconducting quantum circuits for QIP are extremely sensitive, and any undesired noise dissipation can significantly affect their performance [19]. The main source of this dissipation has been attributed to the two-level system (TLS) defects in amorphous dielectrics at surfaces and interfaces of the device[20], specifically contributing to microwave loss at cryogenic working temperatures and single photon power levels. The TLS is an atomic-scale defect with two nearly energetically equivalent configurations or states [21]. When the energy difference between the two states of a TLS matches the microwave frequencies used in quantum circuits, it can strongly interact with the circuit, ultimately leading to decoherence. This power dependence distinguishes TLS losses from other non-TLS losses, such as those caused by non-equilibrium quasiparticles or magnetic flux noise [18,20,22–26]. Accurately categorizing and understanding various losses, especially differentiating between TLS and non-TLS origins, is of great importance to facilitate the pinpointing of specific material's structural culprits that cause the decoherence. The exploration into the microscopic nature of these defects and strategies to mitigate their effects is ongoing and crucial for the advancement of the field [27].

Superconducting qubits often use niobium (Nb) thin films due to their high critical temperature and excellent surface quality, which allows for precise lithographic patterning of superconducting quantum circuits [28–32]. Extensive efforts have been dedicated to characterizing qubits based on Nb thin films to identify materials-related relaxation channels [24,33–37]. Among these, surfaces and interfaces inside the devices are known as major decoherence sources, hosting TLS defects [6,17,19,20,38–41]. The native amorphous surface oxide on Nb has received significant attention due to its detrimental impact on the internal quality factor (Q_i) of superconducting coplanar waveguide (CPW) resonators or superconducting radiofrequency (SRF) cavities [24,36,41–45]. The native surface oxide evolves as Nb_2O_5-NbO_2-NbO-Nb [24,34,46]. Notably, Nb_2O_5 stands out as the primary source of TLS, contributing to microwave dissipation [36,44]. Furthermore, non-stoichiometric defective surface oxides introduce magnetic disorder, resulting in surface impedance loss, commonly referred to as non-TLS loss [15,32]. In addition to these loss components, the Nb-substrate interface is another decoherence channel in superconducting resonators. Given that the fabrication process of superconducting quantum circuits heavily relies on well-established semiconductor workflow, the use of high-resistive silicon (Si) substrates is useful for the large-scale deployment of low-loss superconducting circuits [47]. The loss tangent of the Nb-Si interface is relatively low compared to the Nb-air interface (oxide surface) [41]. However, a recent study demonstrated that the Nb-Si heterointerface could exhibit antiferromagnetism, possibly acting as a dissipation channel [48]. Once the Nb-substrate interface is formed during the qubit fabrication process, there are limited options available to mitigate the associated loss. As a result, fewer research efforts have been dedicated to investigating the Nb-substrate interface compared to the Nb-O surface [35,49,50]. However, the much lower Q_i in Nb CPW resonators than Nb SRF cavities suggests that the nanostructure of the Nb films, Nb/substrate interface, and air/substrate are also the main contributors to their losses [41,44].

This paper aims to clarify the relationship between the deposition method, grain structure, superconducting states, and device performance of Nb film fabricated by high-power impulse magnetron sputtering (HiPIMS) and direct current (DC) sputtering. A combination of characterization techniques,

including advanced electron microscopy and spectroscopy, secondary ion mass spectrometry, magneto-optical imaging, and pump-probe spectroscopy are employed to correlate the microstructure and properties from a multiscale perspective. Through correlating microstructures of Nb film to their residual resistance ratio (RRR), superconducting order parameters, quasiparticle density, and resonator internal quality factor (Q_i), we elucidate how different types of structural defects, including interfaces and grain boundaries, impact the decoherence of superconducting quantum circuits in terms of TLS and non-TLS losses. Our systematic investigation clarifies material-based loss mechanisms and provides valuable insights that can guide the optimization of superconductor thin film deposition for qubit performance enhancement.

2. Experimental details

The Nb films used in this study were deposited on high-resistivity Si wafers ($\rho \geq 10$ kΩ.cm) using physical vapor deposition (PVD) for the fabrication of CPW resonators. Three different PVD conditions were employed to deposit the Nb thin film on Si substrates. The first sample was fabricated using HiPIMS (labeled as **sample A**). The other two samples were fabricated using DC sputtering with variations of power: Low-high power (labeled as **sample B**) and High power (labeled as **sample C**). For samples A, B, and C, the same 5:1 BOE dip and pretreatment procedure was performed, followed by an *in situ* bake prior to Nb deposition. All Nb sputter targets are of 99.999% purity and the same nominal film thickness of 175 nm was targeted for the three samples. Both the HiPIMS and DC sputter processes utilized the same rotation and argon pressure. The HiPIMS process used an 850 V voltage pulse with a low 1% duty cycle. For the DC samples we selected 75 W for the low power and 350 W for the high power set points, respectively for sample B, and sample C. The HiPIMS approximate resulting deposition rate is ~5.1 nm/min, while the DC low power deposition rate is ~5.3 nm/min and DC high power deposition rate is ~25 nm/min. Sample B has approximately 30 nm thickness deposited at low power with the remaining thickness deposited using the high power set point. The low power setpoint was chosen to approximate the deposition rate of the HiPIMS settings. The CPW resonator device structures were patterned from these Nb films using standard

photolithography and reactive ion etching techniques to fabricate inductively-coupled λ/4 resonators with 5 μm gap and 10 μm center trace width [16].

Scanning electron microscopy (SEM) images were collected using Helios (Thermo Fisher Scientific Ltd). Cross-sectional transmission electron microscope (TEM) samples were prepared by a focused ion beam instrument with a gas injection system (Helios, Thermo Fisher Scientific Ltd.). The TEM samples were thinned to electron beam transparency. Plan-view TEM samples for Nb thin films were prepared by mechanical polishing using Multiprep, followed by low energy Ar^+ ion beam milling using Precision ion polishing system 2 (PIPS2). The TEM samples were investigated by an aberration-corrected TEM (Titan Cube, Thermo Fisher Scientific Ltd.) at 200 kV. Energy-dispersive X-ray spectroscopy (EDS) and electron energy-loss spectroscopy (EELS) studies were carried out with a Super-X EDX detector and GIF Quantum ER (965) system, respectively. Transmission Kikuchi diffraction (TKD) was carried out for the plan-view samples in a SEM system (Teneo, Thermo Fisher Scientific, Ltd) equipped with an electron backscatter diffraction detector.

Time-of-flight secondary ion mass spectrometry (ToF-SIMS) measurements were performed using a dual beam IONTOF 5 system to analyze the concentration and depth distribution of impurities in the Nb films. Secondary ion measurements were performed using a liquid bismuth ion beam (Bi+). A cesium ion gun with an energy of 500 eV was used for sputtering the surface for depth profile measurements.

Residual resistivity ratio (RRR) values were obtained by measuring the four-point resistivity of a patterned cross-bridge sheet resistor test bar structure with a length of 370 μm and width of 30 μm as a function of temperature. Test structures were wire bonded to a printed circuit board and thermally anchored to a cryostat with a base temperature of 4 K. We applied 100 μA current across outer contact pads and measured voltage across inner contact pads. RRR value is the ratio of resistivity at 290 K to that at 10 K, just above the expected Nb superconducting transition temperature.

Cryogenic microwave measurements were performed in a dilution refrigerator at a base temperature of 10 mK. The patterned devices were attached and wire bonded to a printed circuit board anchored to the mixing chamber plate and shielded with superconducting and cryoperm cans. The input signal line has a total attenuation of -76 dB and a 7.65 GHz low-pass filter. The output signal line is filtered by isolators and amplified by a high electron mobility transistor at 4 K. Measurements were performed in the S21 configuration, with the output power from the instrument varied between high (+9 dBm) and low (-86 dBm) setpoints. The power is converted to an assumed device occupancy using the measured attenuation, but these values are not calibrated. The measured S21 transmission coefficient is fit to a single pole model in the complex plane and fitted using the method described in [18]. Resonance frequencies are in the 5.2-5.8 GHz range and coupling quality (Q_c) varies from 1×10^5 to 3×10^5, designed to be within a factor of 10 of the Q_i for low error measurements. All low-power Q_i measurements reported are with an average device occupancy $\langle n \rangle \approx 10^{-1}$, low enough so that Q_i is leveled off at a minimum (where TLS loss dominates). The power-dependent Q_i spectrum is fit using the method described in[18] in order to extract the separate contributions of TLS loss from quasiparticles and power-independent loss. This value is expressed in terms of $F*\delta_{tls}$, where we do not make an assumption for the fill factor (F), and δ_{tls} is the sum of TLS loss contributions in the resonator. All high-power Q_i measurements reported are with an average device occupancy $\langle n \rangle \approx 10^8$. We also define a power-independent or high-power loss as $\delta_{HP} = 1/Q_i$ with an average device occupancy $\langle n \rangle \approx 10^8$.

Magneto-optical (MO) imaging was performed in a 4He closed-cycle cryostat using Faraday rotation of linearly polarized light in a bismuth-doped iron-garnet ferrimagnetic indicator film with in-plane magnetization. Perpendicular to the sample surface (out-of-plane) component of the magnetic induction, the perpendicular field (Bz) penetrates the indicator film and polarizes its magnetization. Linearly polarized light propagates through the optically transparent indicator and reflects from the mirror sputtered on its bottom part. The light experiences double Faraday rotation proportional to the local magnitude of the out-of-plane component of the magnetic induction on the sample surface. The spatial resolution of the technique

is about 3 μm. In all images, the brightness level is proportional to the local value of Bz. Samples are placed on a gold-plated copper cold finger with some Apiezon-N (cryogenic) grease. The indicator is placed freely on top. A more detailed description of the technique can be found elsewhere [51].

Ultrafast pump-probe reflectivity spectroscopy is used to measure reflectivity change (ΔR/R) induced by ultrashort laser pulses in sample A (HiPIMS), sample B (DC low-high power), and sample C (DC high power). Samples were mounted on a cold finger having a small hole (diameter ~2mm). The ΔR/R is directly proportional to pump-induced alterations in the superconducting order parameter. Our experimental setup is reflection geometry with a femtosecond fiber amplifier that generates pulses with a duration of 35 femtoseconds and a repetition rate of 40 megahertz. The laser output, operating at a wavelength of 1.5 μm, is split into pump and probe beams. The probe beam is subsequently frequency-doubled to 750 nm and precisely focused onto the samples using a 4-inch focal length lens, all in a collinear geometry. The pump fluence is maintained at 3 μJ/cm², while the probe fluence is set at 0.3 μJ/cm². To measure the pump-induced reflectivity changes, we employed a lock-in amplifier with a 40 kHz modulation of the pump beam. Our Nb thin film samples, representing both HiPIMS and DC samples, were securely clamped between indium foils with 2 mm apertures and the cold finger of a magnetic cryostat. The indium foil is thermally connected to the cold finger through an additional copper plate to ensure accurate temperature control of the Nb sample. Additionally, we applied a perpendicular magnetic field to the sample surface to complete our experimental setup and measure the magnetic screening of superconducting states.

3. Results and Discussion

High Power Impulse Magnetron Sputtering (HiPIMS) is a newer and increasingly popular method for fabricating superconducting thin films. It is a variant of direct current (DC) sputtering [52]. HiPIMS uses short, high-voltage pulses of electrical power to create high-density plasma in the sputtering chamber [53], offering several advantages, such as higher density, improved adhesion, improved topographic coverage, and in some cases, reduced defects and smoother films over traditional sputtering methods [54].

A study by Premkumar et al. [37] provided a systematic insight into the correlations between microscopic materials properties and qubit performance. It also emphasized the crucial role of suboxides at the surfaces and grain boundaries of Nb thin film in the transmon qubits by comparing different deposition methods for Nb thin films [37]. However, understanding of the intrinsic structure of polycrystalline film and differences in surface and interfaces to different deposition methods remains limited [9]. The main goal of this study is to fill this above knowledge gap.

3.1. Nb films' surface morphology

The surface roughness of the HiPIMS-deposited Nb film (sample A) is more pronounced compared to the other two films deposited by DC sputtering, as demonstrated in SEM surface images (Figs. 1a-c). In addition, high-resolution SEM images show an elongated hill-shaped surface morphology for all films (Figs. 1d-f), but sample A displays a higher contrast between hills and valleys compared to the other two sputtered films, suggesting a larger height difference between these surface features in sample A. Atomic force microscopy (AFM) images reveal that the root-mean-square (RMS) surface roughness is ~0.58 nm for sample A, ~0.43 nm for sample B, and ~0.37 nm for sample C (Details in **Supplementary Material.**). Details are revealed in the TEM cross-section images discussed below.

3.2. Nb films' surface oxides

Sample A exhibits a thicker and more uneven surface oxide layer with a greater variation in thickness compared to the other two DC-sputtered films. However, there is no noticeable difference in the surface oxide morphology between samples B and C. Variability in surface roughness is evident in the cross-section TEM images presented in Fig. 2, where the Nb film thickness of the three samples is nearly identical. sample A and C have a Nb thickness of ~175 nm, while sample B has a Nb thickness of ~185 nm (Figs. 2a, d, and g).

Grain boundary grooving with enhanced oxygen diffusion into the boundaries may influence the surface microstructure, resulting in larger variations in surface oxide thickness. The HAADF-STEM images

and corresponding EDS elemental distribution maps of Nb and O at the air-Nb interfaces of the three samples show that sample A has a thicker oxide layer of up to ~9 nm at the valley regions (Figs. 2b-c) which typically occurs where the grain boundaries meet the free surface. This is consistent with ToF-SIMS measurement results, which show the decay length of the oxygen counts (depth over which the counts stabilize to a bulk value) in the ToF-SIMS data is longer for the HiPIMS sample than two DC sputtered samples (Details in **Supplementary Material**). This surface oxide layer with larger thickness variation can have a negative impact on the resonators' Q_i as a TLS loss source. However, it is worth mentioning that the waviness of the Nb surface is not solely attributed to grain size and grain boundary grooving, as some valleys do not form at grain boundaries. Moreover, spatially resolved EELS analysis demonstrates that all samples exhibit similar surface oxide chemistry with nearly identical gradual changes in Nb valence states across the amorphous layers (Details in **Supplementary Material**), consistent with our earlier study [34].

The elongated features in the amorphous surface oxides are analyzed from the plan-view TEM sample. Fig. 3 shows plan-view STEM micrographs, which include O and Nb elemental distribution maps, as well as EEL spectra from the region of interest. In Fig. 3a, the HAADF-STEM micrograph of the surface oxides exhibits similar surface features to those in SEM images in Fig. 1. The contrast in the HAADF-STEM image primarily arises from variation in the total thickness of the TEM sample. EELS elemental composition maps of O and Nb reveal that the brighter region observed in the HAADF-STEM micrograph, corresponding to the thicker region, exhibits lower oxygen and higher niobium concentration compared to the darker region in the HAADF-STEM image (Figs. 3a-c). Because the plan-view samples were prepared by Ar^+ ion milling from the substrate side, the thicker regions should correspond to the hill-like features observed in the SEM image. Thus, the thicker region may have a larger portion of lower valence niobium oxides, as depicted in Figs. 3b-c with a high Nb atomic percentage. This trend is also evident in the EELS analysis on the Nb M_{23} edge. Fig. 3d demonstrates that the energy position of the Nb M_3 peak taken from spot 1 in Fig. 3a (from the region that has a darker contrast in the HAADF-STEM image) is higher than that from spot 2 (from the region that has a brighter contrast in the HAADF-STEM image). A dashed line

at 365 eV in Fig. 3d indicates the peak produced at the energy loss corresponding to Nb^{5+}, and lower energy peaks than 365 eV representing lower oxidation states [34,55]. This EELS analysis demonstrates that the thicker Nb oxide region consists of a larger volume fraction of suboxides.

3.3. Grain size of Nb films

The plan-view bright field TEM images in Figs. 4a-c reveal that all the grains in the Nb films appear to have an equiaxed shape, rather than being elongated. Therefore, elongated surface features observed in SEM images are not directly related to the lateral grain shape, which implies that directly correlating the surface morphology of the film to grain size might be misleading [56], as also demonstrated elsewhere [57]. We suspect that the elongated surface feature may follow a specific crystallographic orientation. The average grain size of sample A is measured to be 44.0 $\pm$ 13.8 nm, which is significantly smaller than the average grain sizes of the DC sputtered samples, which are 68.8 ± 25.2 nm and 65.3 ± 21.6 nm for sample B and C, respectively (Figs. 4d-f and Table. 1). Furthermore, the plan-view samples exhibit arc-shaped features in the selected area diffraction (SAD) patterns (insets in Figs. 4d-f), which are formed by the intersection of inclined reciprocal rings with the Ewald sphere [58,59]. Those arcs of diffraction spots indicate the presence of texture in the Nb films [34,60]. To analyze the texture orientation in the Nb films, we performed SEM-TKD to obtain pole figures (Figs. 4g-i). In all the samples, strong intensities are observed at the center of the {110} pole figure with ring-shape intensities around the center. These intensities have a similar degree of maximum multiples of uniform density (MUD) of ~20. However, there is no texture intensity at the center of {100} and {111} pole figures. The presence of the centered texture intensity in the pole figures indicates the corresponding textures along the z-direction of the plan-view samples. Therefore, all the films exhibit a strong {110} texture, which is a common texture in BCC metal film, resulting from surface energy minimization. There is no mixture of {100} or {111} textures.

The average lateral grain size of Nb is closely associated with the total volume of the enhanced oxygen diffusion region into the Nb film. This is because grain boundaries and triple junctions can act as

channels for oxygen diffusion [61]. Consequently, smaller grain size gives rise to a larger volume of grain boundaries and triple junctions per unit area, which may host a higher density of TLS due to higher Nb-oxide content [20,27]. Direct observation of oxygen localized at the grain boundaries and triple junctions is presented in Fig.5. In the atomic resolution HAADF-STEM plan-view image of sample C (Fig. 5a), spot 2 from the grain boundaries, and spot 3 from triple junctions clearly exhibited the characteristic of O K edges at approximately 530 eV (Fig. 5b), in contrast to intra grain area (spot 1). It is worth noting that the triple junction has a higher O content than the grain boundary. This observation provides compelling evidence of higher oxygen content at the grain boundaries and triple junctions of the Nb film, revealing a relationship between the Nb grain size and the potential source of TLS.

3.4. Nb-Si interface

Close analysis at the Nb/Si interface shows no epitaxial relationship between Si and Nb. Instead, there are two layers between the Nb film and the Si substrate, labeled as layer 1 (L1) and layer 2 (L2) in the high-resolution HAADF-STEM micrograph and corresponding EDS elemental mapping shown in Figs. 6a-c. L1 lacks any lattice fringes, while L2 retains the Si lattice fringes but is less distinct. Based on contrast and lattice fringes of HAADF-STEM micrograph in Figs. 6a-c, the results show that sample A has an L1 of ~2 nm and an L2 of ~4.5 nm, while both sputtered films (sample B and C) have an L1 of ~1.5 nm and an L2 of ~6.5 nm. This implies that the difference in deposition rate doesn't noticeably affect the thickness of the interface layer at the Nb-Si interface between DC-sputtered films (sample B and C). It is worth noting that both interface layers exhibit a linear composition change with different slopes based on the extracted EDS line profiles of Nb and Si composition for all samples shown in Fig. 6d-f. The two layers can be distinguished based on where the abrupt change in the Nb:Si occurs within the interfacial region. Based on the slope difference in EDS line profiles, the results show that Sample A has an L1 of ~4 nm and an L2 of ~5 nm, while both DC magnetron sputtered films (sample B and C) have an L1 of ~3 nm and an L2 of ~7 nm, which are slightly larger than the measured L1 and L2 thickness based on HAADF-STEM micrograph. Furthermore, although the thickness of the L1 and L2 layers between sample A and the DC sputtered films

(sample B and C) is different, the composition at the L1/L2 interface (the point when the slope changes in the extracted EDS line profile) are nearly identical (~17 at% Nb and 83 at% Si), as indicated by blue arrows in Figs. 6d-f. Thus, the general composition profiles of L1 and L2 remain the same regardless of the deposition techniques but the actual gradients differ. The average composition of the amorphous L1 layer is approximately consistent with the stoichiometry between Nb_5Si_3 and Nb_6Si_5, which are the two most stable phases among ultrathin intermetallic niobium silicides [48]. The retention of the Si lattice and abrupt change in the Nb:Si between L1 and L2 suggests a possible overlap of NbSi amorphous phase and Si substrate along the STEM electron beam direction in the L2 layer.

No obvious difference in electronic structures of Nb and Si across the Nb-Si interface between sample A and the DC sputtered films (sample B and C) was observed despite the thickness difference in silicide interface layers. More details are shown in **Supplementary Material.** Due to the higher incident power involved in HiPIMS deposition relative to the DC sputter techniques, Nb can implant into or cause amorphization of the Si substrate more deeply, resulting in the formation of a thicker amorphous interface layer, as shown in Fig.6 and in **Supplementary Material**. A similar effect was observed by Kopas et al. [49] correlating Si surface defect depth with Ar ion mill energy. The consistency in the composition of the two layers and the agreement in the EELS results suggest that the amorphous structures with measured chemistry are thermodynamically favored. Amorphous Nb–Si alloys can be formed using a number of rapid quenching techniques [62–64], including sputtering [65]. Rapid quenching of Nb-near the 18.7 at.% Si eutectic composition can result in the formation of metallic glass [66]. It is well established that metallic glasses tend to form in the vicinity of deep eutectics [67], and the compositions here fulfill this criterion, being close to the eutectics at 57% and 98% Si [68].

3.5. Relationship between deposition method, microstructure, and device performance

The Nb film superconducting transport properties and the fabricated 2-D waveguide resonator performance are directly influenced by the microstructure of the thin films, which are determined by

different deposition methods. As shown in Table. 1, sample A exhibits a lower RRR of 4.55 ± 0.1 compared to the RRRs of samples B and C, which are 6.66 ± 0.1 and 6.53 ± 0.1, respectively. The lower RRR of sample A may be attributed to its smaller average grain size of 44.0 ± 13.8 nm, approximately 50% smaller than the average grain sizes in samples B and C. A polycrystalline film with a smaller grain size has a larger volume fraction of grain boundaries and triple junctions, which can act as a weak Josephson junction barrier negatively impacting the thin film's surface resistance [37,69].

The low power median Q_i value of the HiPIMS resonators is lower at 170000 ± 116000 compared to the Q_i values of samples B and C, which are 311000 ± 226000 and 983000 ± 318000, respectively, as shown in Fig. 7a and Table. 1, where the errors are the standard deviation of each distribution. After extracting the TLS loss contribution from the power-dependent Q_i sweeps (shown in Fig. 7c), we observe that TLS loss fit values may inversely correlate with RRR since the TLS loss is one of the dominant sources of losses in a superconducting qubit. This finding seems to align with the claim by Premkumar et al. that RRR may be used as an indicator of qubit lifetime [37]. As shown in Fig. 7c, TLS losses of samples B and C are similar, and in these films, we observed a similar grain size and microstructures at the Nb-air surface and Nb-Si interface. TLS loss of sample A is higher compared to samples B and C, demonstrating that the dominant dissipation mechanism is likely from coupling to TLS defects in the amorphous dielectrics at the surface, interfaces, and intergrain regions close to the surface. The specific microstructural factor contributing to the difference in high power Q_i values (Fig. 7b) between sample B and C may be attributed to microstructure differences stemming from crystalline inhomogeneity (e.g., the difference in initial deposition rate between sample B and C, and discontinuous thin film growth of sample B), which may lead to non-TLS losses (Fig. 7d). As shown in Fig. 2d, this microstructural feature in sample B is observed by diffraction contrast, showing that higher defect density in the lower part of the Nb thin film is indicated by the yellow arrow.

Another potential source of loss is that the thicker niobium silicide in sample A may introduce magnetic instability, potentially acting as a dissipation channel. Lu et al. [48] predicted that niobium silicide

nanofilms have two stable compositions: α-Nb_5Si_3 for the thicker film and Nb_6Si_5 for thinner films. The critical thickness for the transition between the two compositions is approximately 1.2 nm. As the thickness of L1 in sample A is larger than the critical thickness (Figs. 6a and S4a), the composition of L1 is likely close to the α-Nb_5Si_3 phase, and it may exhibit antiferromagnetic properties [48]. While the intrinsic antiferromagnetic order, when perfectly balanced, would not be a source of magnetic flux noise, the imperfections or dynamics associated with real antiferromagnetic materials could act as a 1/f magnetic flux noise source, which ultimately negatively impacts the Q_i value. On the other hand, the thickness of L1 in samples B and C is approximately 1.5 nm (Figs. 6b-c and S4d,g), suggesting that this layer may consist of nonmagnetic Nb_6Si_5, which might be less detrimental to the resonator performance. Therefore, the thicker amorphous Nb silicide is a potential source that we are actively investigating for both TLS [20] and non-TLS losses [15,48,70], perhaps further decreasing the low power Q_i value in sample A.

3.6. Magnetic flux penetration of superconducting states

Magnetic flux penetration measurement results are in line with microstructural characterization and microwave measurements. Fig. 8 shows magneto-optical snapshots of the magnetic flux penetration into three films analyzed in this paper. Un-patterned "blank" films were produced under exactly the same conditions as the patterned films used for quality factor measurements. In the left column (Figs. 8a,c,e): the sample was cooled to 4 K, and then a magnetic field of 40 Oe was applied. In the right column (Figs. 8b,d,f): the sample was cooled to 6 K and with a magnetic field of 80 Oe. While during normal operation, transmon will never experience such amplitudes of the magnetic fields, such measurements help to reveal problematic areas and inhomogeneities of the superconducting state. Two morphological properties determine the response in this case.

First, niobium films suffer from thermomagnetic instabilities at low temperatures [71]. Even without the applied magnetic field, it means that the heat removal through the substrate is impeded in films where dendritic avalanches are observed. The domain of avalanche existence is also temperature-

dependent. In the present case, sample A (HiPIMS, Figs. 8a-b) does not show avalanches, sample B (Low-High DC, Figs. 8c-d) shows them both at 4 and 6 K, while sample C (High DC, Figs. 8e-f) only at 4 K. Therefore, sample A has the best heat channeling through the substrate, followed by sample C. This is consistent with the thickest Nb/Si intermix interface in sample A, as shown in Fig.6. It is argued that a thicker Nb silicide has a higher metallicity [48], which might act as a better heat dissipation channel. However, it is also likely that such a thick gradual layer has a negative impact on quantum coherence as the superconducting order parameter is gradually smeared over the thickness of this layer, leading to pairbreaking even by nonmagnetic scattering centers in this inhomogeneous situation.

Second, examining the right column of Fig. 8, it is clear that at the same temperature and magnetic field, the magnetic flux penetrates film A much further than film C (Figs 8b and f). It is unlikely that the bulk pinning inside the grains is significantly different, so this observation may be attributed to a larger fraction of the intergrain material at the grain boundaries in sample A. In granular superconductors, RRR is not a good figure of merit in some cases [71] as it mostly depends on the higher resistance intergrain regions. Indeed, the effective RRR of film A is lower because of the smaller grain size, so the fraction of high resistance boundaries is greater. The intergrain regions have suppressed the order parameter [72], so that, in general, the order parameter is more inhomogeneous in films with smaller grain size, leading to a lower quality factor, apart from the TLS loss mechanism.

Even though the grain size, surface, and interface of samples B and C are almost the same, the magnetic flux penetration measurement results show sample C exhibits better superconductivity. This is in line with better high power Q_i in Sample C, which is mainly attributed to non-TLS loss. The poor superconductivity of sample B might be explained by the discontinuous deposition parameters which perhaps induces a low-quality initial layer and higher density of structural defects at the interface between low-speed and high-speed films, as shown in Fig. 2d. As a result, this leads to inhomogeneities of the superconducting state in the lower part of the Nb thin film, which in turn induces power-independent dissipation channels. Since Fig. 5 only shows the grain size near the top surface of the thin films, this feature

is not observed by the plan-view sample. This is well correlated to the overall Q_i measurement that shows better performance in sample C (Fig. 7e).

To summarize the magneto-optical results: Sample A (HiPIMS) shows the best thermal coupling to the substrate but suffers from small grain size, exhibiting an easy flux penetration into the interior, whereas sample C shows the strongest, most robust superconductivity and better thermal coupling to the substrate, compared to sample B.

3.7. Pump-probe measurements of superconductivity

Ultrafast pump-probe reflectivity spectroscopy is a powerful technique for investigating the superconducting order parameter and quasiparticle dynamics [73]. Fig. 9 shows pump-induced reflectivity spectra changes in superconducting states $(\Delta R/R)_{superconducting}$ for sample A (HiPIMS), sample B (DC low to high) and sample C (DC high power) under a magnetic field. These measurement results align with our findings from magnetic field screening, microstructural characterization, and microwave resonator quality factor measurements. We draw the following three conclusions from the ultrafast pump-probe reflectivity measurements. Since the $\Delta R/R_{superconducting}$ signals are completely suppressed in sample A under an external magnetic field of 600 mT (green trace, Fig. 9a), we conclude that the pump-probe signals in the lower magnetic field traces (red for 0 mT and blue for 400 mT) are primarily attributed to the superconducting condensate and are not significantly influenced by measurement or other pump-induced thermal effects. The latter signals should not exhibit a significant dependence on the applied magnetic field. These data show that the HiPIMS film (sample A (Fig. 9a) exhibits a much more pronounced magnetic field effect with completely suppressed superconducting condensate responses into the normal state. On the contrary, sample B (Fig. 9b) and sample C (Fig. 9c) are not fully suppressed at 600mT, indicating a stronger magnetic screening. These magnetic field-induced changes of condensate dynamics clearly show the existence of more robust superconductivity than sample A. Additionally, the data unequivocally demonstrates a higher quasiparticle generation rate in sample A. This is evidenced by progressively smaller slopes in the log (QP

density) vs. B field plots compared to sample B and sample C (Fig. 9d). This observation aligns with the presence of more heterogeneous grain structures.

We offer a more comprehensive account of the analysis employed. Since the $\Delta R/R_{superconducting}$ signals are directly proportional to the pump-induced change of superconducting condensate density, we can use these signals to extract thermalized quasiparticles using the well-established Rothwarf -Taylor model [74], which helps us comprehend pair breaking induced by pump photons and hot phonons. In this weak perturbation regime, the minimum depletion of the Cooper pairs $\Delta n/ns \ll 1$. Following the Rothwarf and Taylor model, the high-energy photons break a small portion of Cooper pairs immediately and turn them into QPs [75]. These energetic QPs transfer their energy into high-frequency phonons afterward and continue to break cooper pairs to reach a quasi-equilibrium state. For slow decay processes (>> ps), the decay rate of QPs is governed by pair breaking by high-frequency phonons and QP recombination into Cooper pairs. The kinetic equations of QPs and hot phonons are solved under balanced conditions, which leads to $1/(\Delta R/R) - 1$ being proportional to the thermal quasiparticle density. Following this, we can implement the procedure outlined in [76,77]. The quasiparticle density results are presented in Fig. 9d. Notably, sample A exhibits a significantly higher quasiparticle density and a steeper slope in response to the applied magnetic field, in contrast to sample B and sample C. This higher quasiparticle density in sample A suggests the presence of pair-breaking channels, likely stemming from prevalent grain boundaries and interfaces. These findings are consistent with the observations made in our MO and TEM images.

3.8. Classification of the contributions of respective microstructures to different losses

Based on the above experiment, we categorize the predominant microstructural culprits on their individual roles in decoherence mechanisms from the perspective of TLS or non-TLS sources (Table. 2) [24]. It is important to note that TLS and non-TLS sources may influence each other in both direct and indirect manners [20,78]. Subsequently, we explore how deposition methods might influence the emergence of these features during fabrication. The concluding schematic illustration is shown in Fig. 10.

Surface Nb oxides: NbO_x has been identified as detrimental to resonator performance both in terms of TLS and non-TLS loss [24]. While overall amorphous oxides, especially Nb_2O_5, are prevalent sources of TLS losses [36,44], non-stoichiometry pentoxide and suboxides with magnetic impurities could predominantly contribute to non-TLS losses [15,24,32,70,79]. HiPIMS deposition results in smaller grain sizes, leading to an increase in the volume of grain boundaries and triple junctions inside. This, in turn, can cause grain boundary grooving and enhanced oxygen diffusion through the boundaries, resulting in larger thickness variations of the surface oxide layer. As a result, films from HiPIMS deposition may host more TLS and non-TLS loss sources close to the surface region.

Nb-Si interface: This substrate and film interface emerge as a potential source of TLS. The formation of amorphous Nb silicide may host TLS defects [20]. Moreover, as this layer grows thicker, it may give rise to magnetic flux noise [48], further complicating the scenario by acting as a non-TLS source of decoherence. Among the three different samples, deposition power in DC sputtered film doesn't have a significant impact on the thickness of the Nb-Si interface layer; instead, it's the deposition method (huge difference in power density and duty cycle between HiPIMS and DC sputter) that makes the difference.

Grain boundary in Nb thin film: The grain size is directly related to surface oxides volume fraction, as well as oxygen (or other impurities) concentration close to the film surface through enhanced diffusion along grain boundaries and triple junctions. Therefore, grain size is closely related to TLS [37]. In addition, grain boundary-induced crystalline imperfections (dislocations and point defects) might induce spatially inhomogeneous superconducting order parameters, broadening the quasiparticle density of states and subgap states, directly connected to power-independent impedance loss [72]. Since a higher density of quasiparticles results in resistive losses, and the grain boundary acts as a weak Josephson junction [37,69], grain boundaries also may contribute to non-TLS losses. It is noteworthy that nonuniform deposition methods (sample B) may induce more crystalline defects and inhomogeneities of the superconducting state, further leading to power-independent non-TLS losses. Although we observed suspicious microstructural features originating from discontinuous deposition conditions, the precise characterization of these losses at the microstructural level remains an underexplored domain, signaling the need for

comprehensive investigations. The exact magnitude and mechanism through which these losses impact superconducting circuit performance warrant a deeper dive.

4. Conclusions

A systematic investigation of the impact of deposition methods and conditions on intrinsic microstructure, film superconductivity, and device performance clarifies decoherence mechanisms from different interfaces and defects in Nb film. In comparison to the DC-sputtered Nb films, the HiPIMS Nb film exhibits a smaller grain size, thicker surface oxide with greater thickness variation, and a thicker amorphous silicide layer at the Nb/Si interface. These structural differences directly correlate with the reduced RRR of the thin films and the TLS loss fit from the power-dependent internal quality factor (Q_i) of the resonators produced. Moreover, the high power DC sputtered film shows the strongest and the most robust superconductivity, despite a higher concentration of O and C impurities inside. Our investigation revealed that amorphous Nb surface oxides, Nb silicide layer, and interstitials (such as oxygen) along grain boundaries can host TLS losses, while non-stoichiometric Nb pentoxide and suboxides and antiferromagnetic materials residing in Nb silicide, and crystalline defects such as grain boundaries can host non-TLS losses. In addition, crystalline imperfections from discontinuous deposition conditions contribute to non-TLS loss. These experimental findings lead to the conclusion that Nb metal with larger grains without surface oxides, ideally monodomain epitaxial films with sharp substrate/niobium interface, are needed to mitigate both TLS and non-TLS losses for the highest-Q resonators.

Acknowledgments

This work was supported by the U.S. Department of Energy, Office of Science, National Quantum Information Science Research Centers, Superconducting Quantum Materials and Systems Center (SQMS) under contract No. DE-AC02-07CH11359. All electron microscopy and related work were performed using

instruments in the Sensitive Instrument Facility in Ames Lab. The Ames Laboratory is operated for the U.S. Department of Energy by Iowa State University under Contract No. DE-AC02-07CH11358. We thank the Rigetti fab team members for the processing development and fabrication of studied specimens.

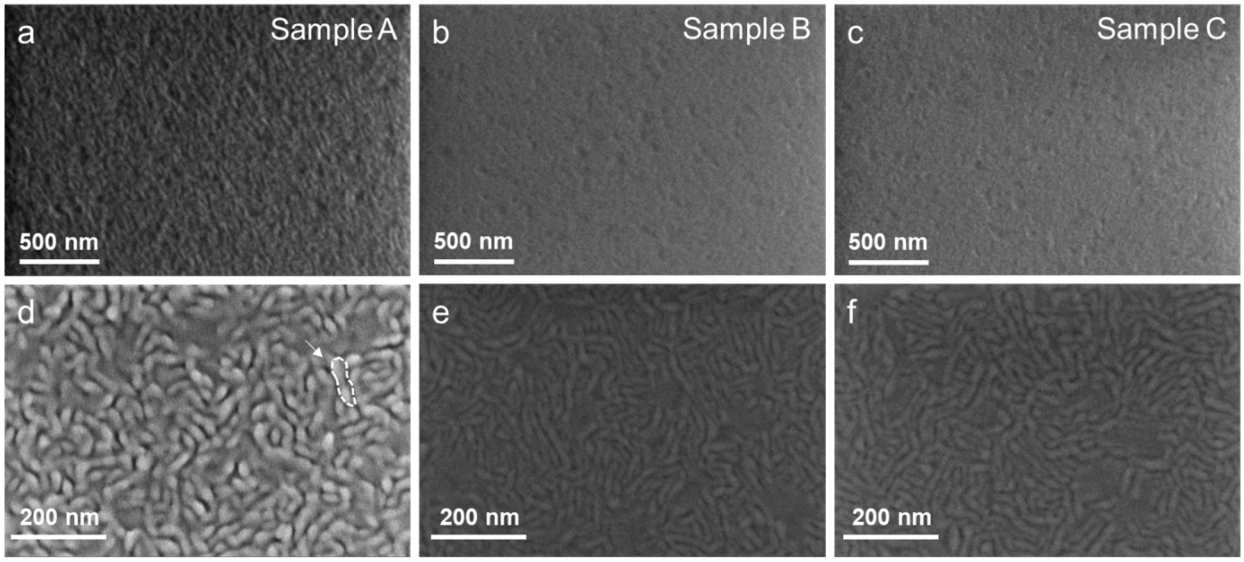

Fig. 1. SEM images of Nb thin film surface from samples A-C. High-resolution secondary electron images of **(a,d)** sample A, **(b,e)** sample B, and **(c,f)** sample C. An example of the elongated surface feature is indicated by the white outline.

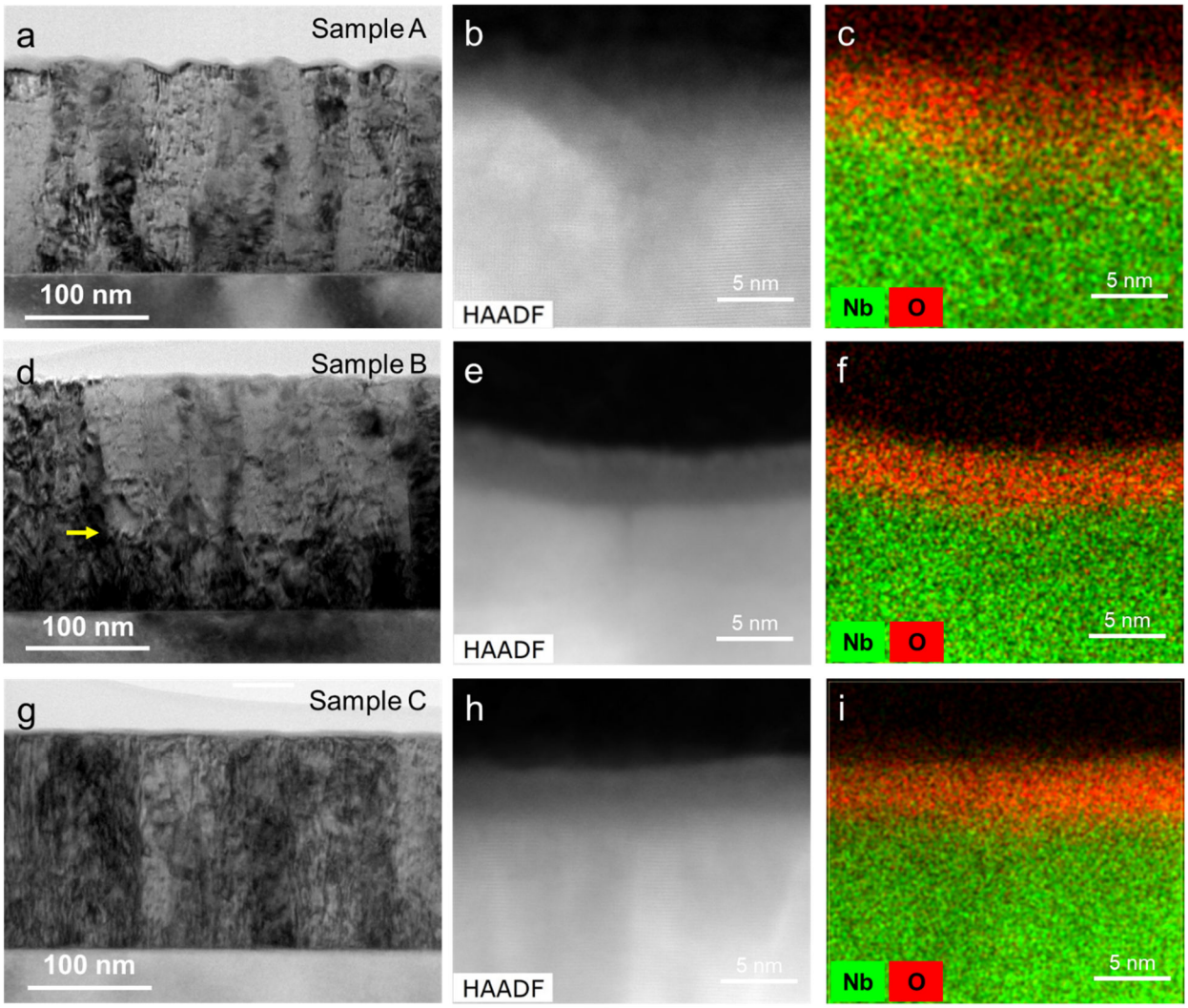

Fig. 2. Cross-sectional and plan-view (S)TEM images with chemical information of sample A-C. (a) Cross-sectional bright-field image, **(b)** HAADF-STEM image, and **(c)** corresponding EDS elemental distribution map of O and Nb at the NbO_x-Nb interface of sample A. **(d)** Cross-sectional bright-field image, **(e)** HAADF-STEM image, and **(f)** corresponding EDS elemental distribution map of O and Nb at the NbO_x-Nb interface of sample B. Yellow arrow in **(d)** denotes a structural inhomogeneity originating from discontinuous deposition condition of sample B. **(g)** Cross-sectional bright-field image, **(h)** HAADF-STEM image, and **(i)** corresponding EDS elemental distribution map of O and Nb at the NbO_x-Nb interface of sample C. Nb thin film deposited by HiPIMS shows a thicker NbO_x layer and obvious surface roughness.

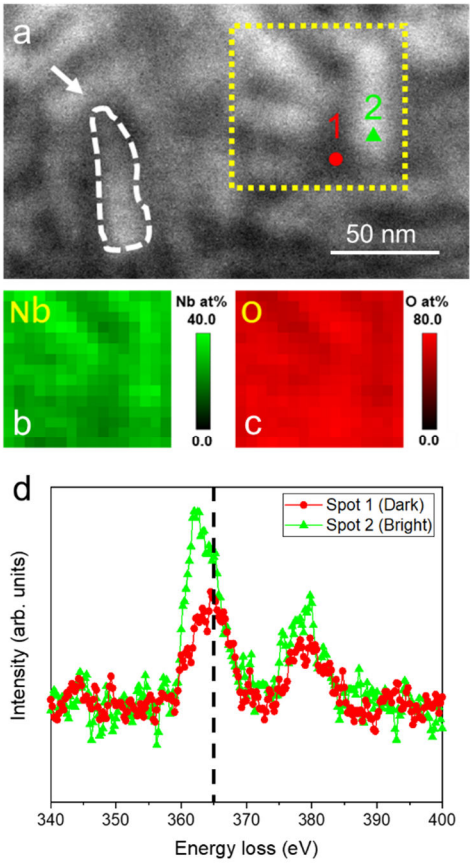

Fig. 3. **Amorphous surface oxides of Nb region from the plan-view sample of sample C. (a)** HAADF-STEM micrograph of the surface oxide region of the plan-view sample. An example of the elongated surface feature is indicated by a white arrow. **(b-c)** Niobium and Oxygen composition maps taken from the region denoted by the dotted yellow box in **(a)**. The brighter region in the HAADF-STEM micrograph corresponds to a higher concentration of Nb than the darker region. **(d)** EEL spectra showing ELNESs of Nb M_{23} edge acquired from positions indicated by spots 1-2 in **(a)**. The brighter region in the HAADF-STEM micrograph corresponds to the lower valence states of Nb than the darker region.

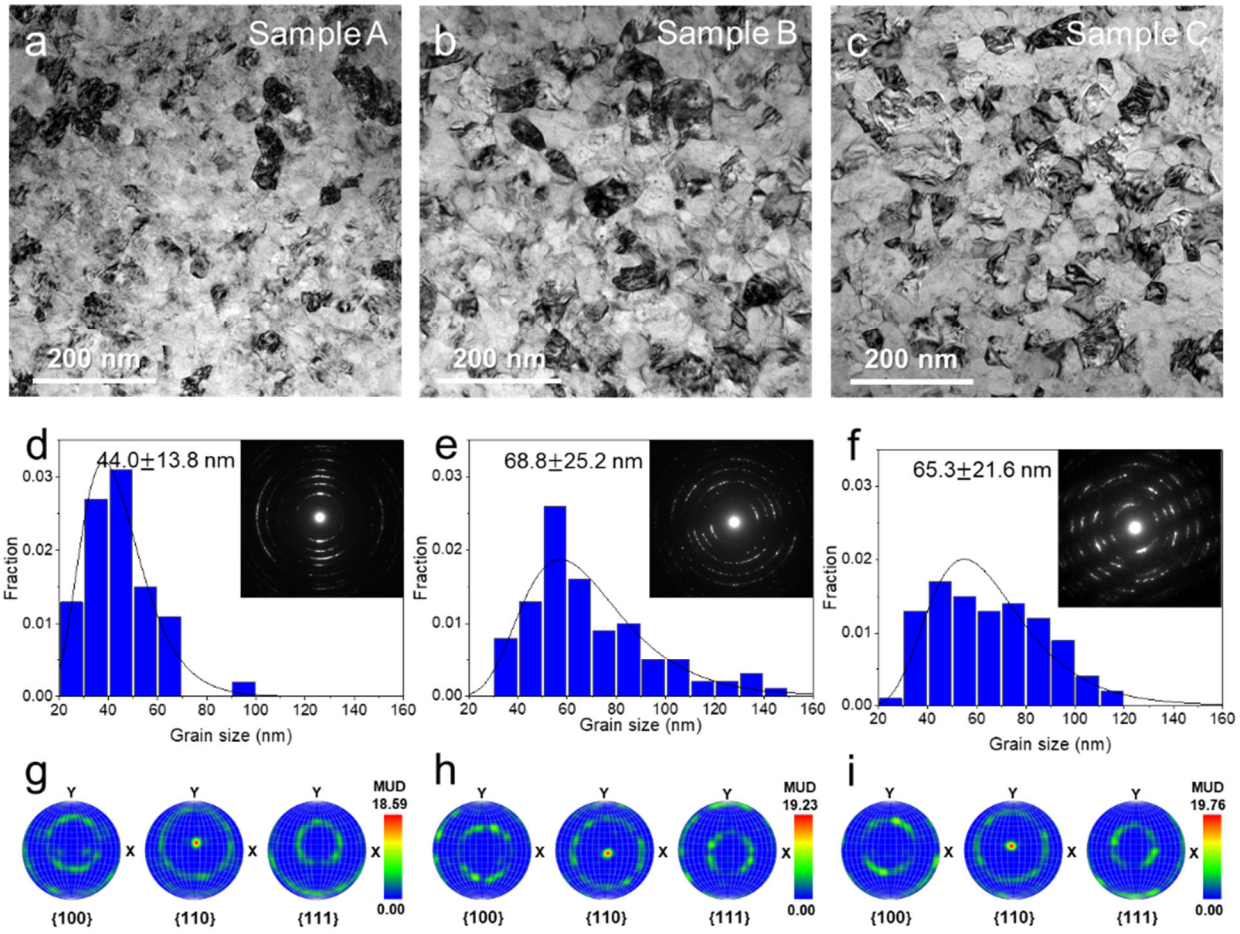

Fig. 4. Plan-view (S)TEM images, grain size distribution, diffraction patterns, and pole-figures of sample A-C. (a-c) Bright-field TEM images of samples A, B, and C. **(d-f)** Distribution of lateral grain sizes of samples A, B, and C. The numbers in the graphs indicate the average lateral grain size of Nb. Inset: selected area electron diffraction patterns. Diffraction patterns from all samples show arc-shaped features, indicative of textured thin film. **(g-i)** {100}, {110}, and {111} pole figures of samples A, B, and C. All of the pole figures were obtained using SEM-TKD.

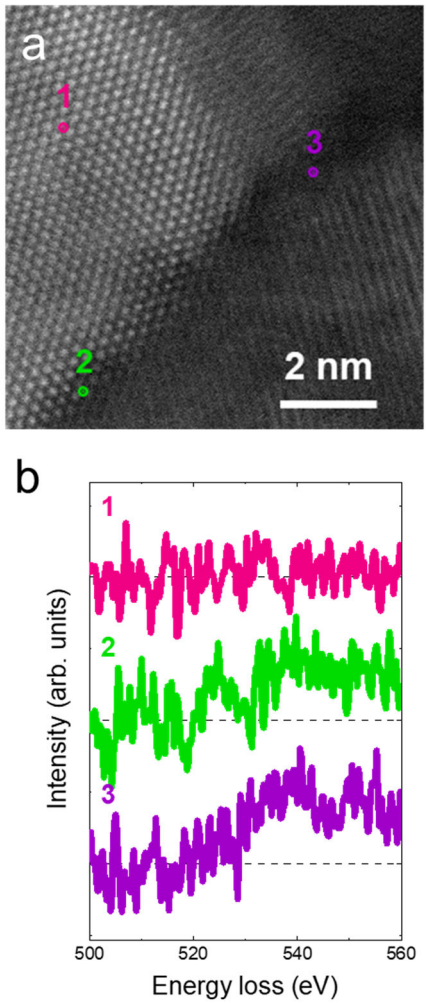

Fig. 5. Localized oxygen at the grain boundaries and triple junction. (a) Atomic resolution HAADF-STEM micrograph of Nb plan-view sample of sample C. **(b)** Oxygen K edges taken from the spots 1-3 indicated by colored spots in **(a)**. Spots 2 and 3 show an increase in counts over the background at 532 eV consistent with the Oxygen K-edge, indicating that oxygen preferentially diffused along grain boundaries and triple junctions. Note that the triple junction has higher Oxygen content than the grain boundary.

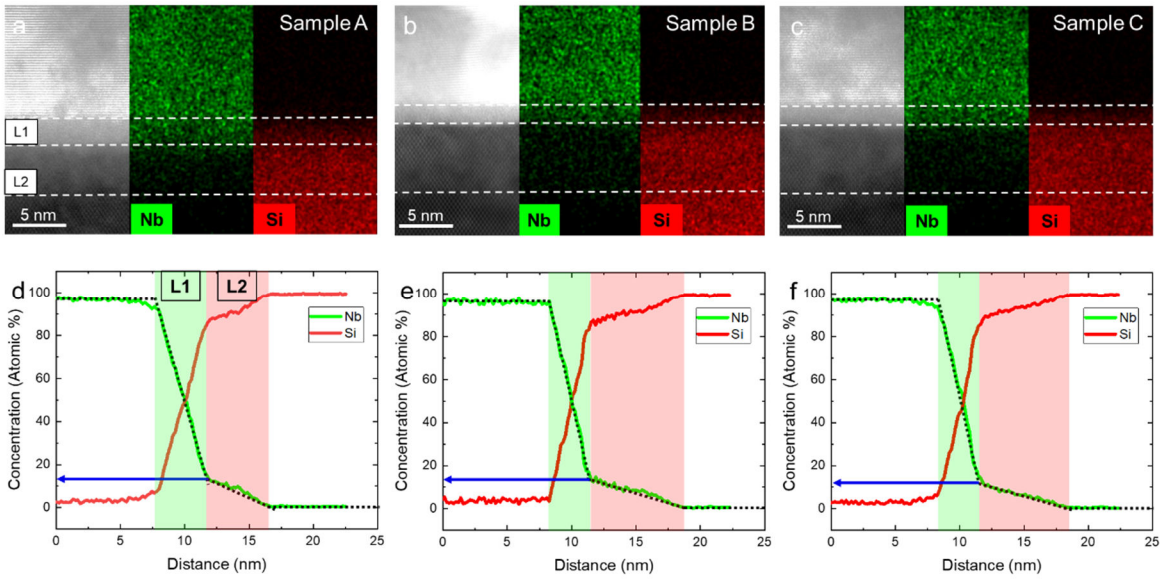

Fig. 6. EDS elemental distribution map and extracted EDS line profiles of Nb-Si interface of samples A-C. HAADF-STEM image and corresponding EDS elemental distribution maps of Nb and Si at the Nb-Si interface of **(a)** sample A, **(b)** sample B, and **(c)** sample C. Line profile of Nb and O concentration across the Nb-Si interface of **(d)** sample A, **(e)** sample B, and **(f)** sample C. Layer 1 is thicker in sample A than in samples B and C, while Layer 2 is thinner in Sample A. The thickness of the two layers is almost identical between sample B and C. Note that the concentration at the transition between Layer 1 and Layer 2 is identical regardless of deposition methods and conditions, as indicated by solid blue arrows in **(d-f)**.

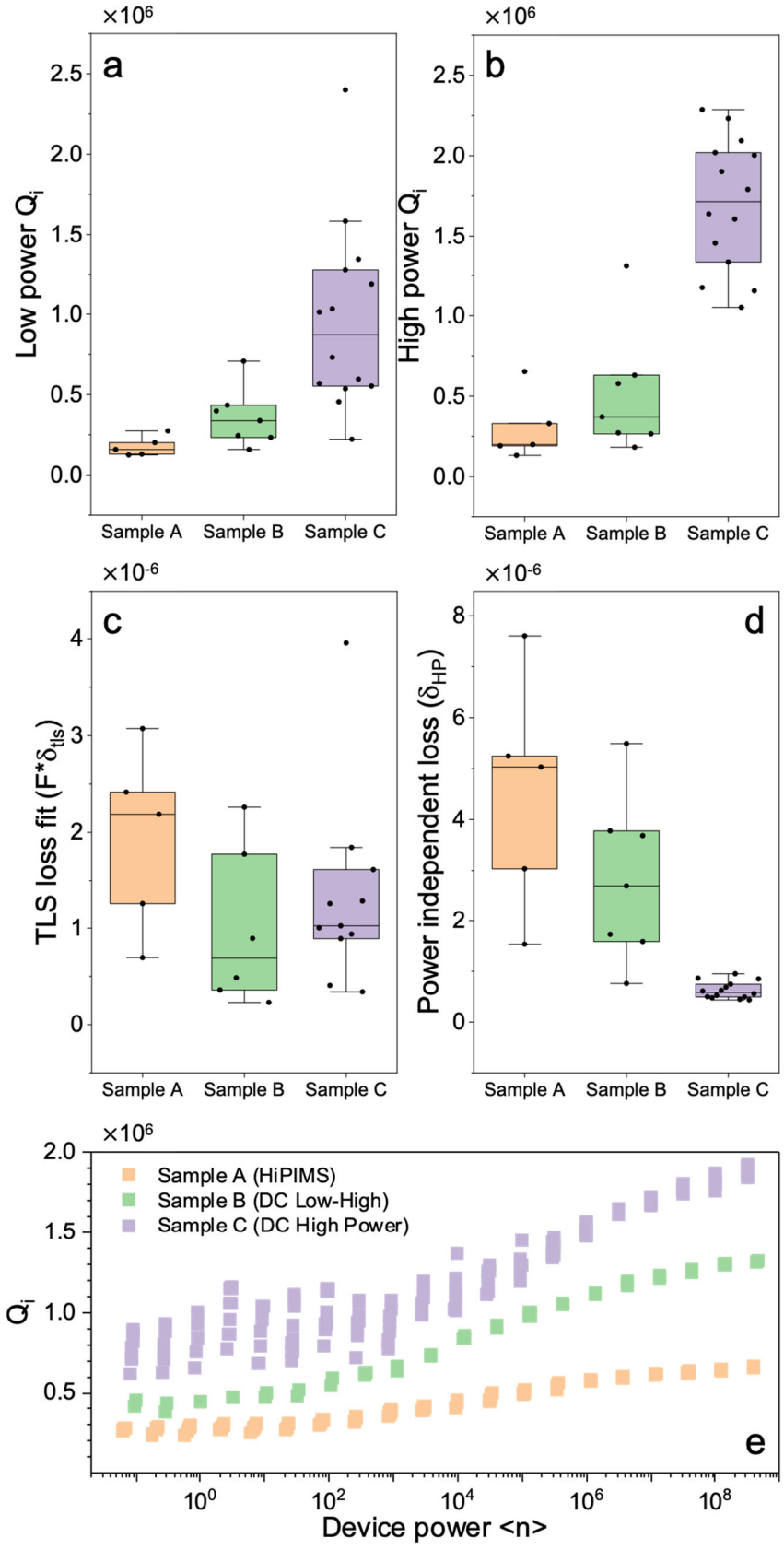
×10⁶
a
Low power Qi
2.5
2.0
1.5
1.0
0.5
0.0
Sample A
Sample B
Sample C
×10⁶
b
High power Qi
2.5
2.0
1.5
1.0
0.5
0.0
Sample A
Sample B
Sample C
×10⁻⁶
c
TLS loss fit (F*δtls)
4
3
2
1
0
Sample A
Sample B
Sample C
×10⁻⁶
d
Power independent loss (δHP)
8
6
4
2
0
Sample A
Sample B
Sample C
×10⁶
Sample A (HiPIMS)
Sample B (DC Low-High)
Sample C (DC High Power)
Qi
2.0
1.5
1.0
0.5
e
10⁰
10²
10⁴
10⁶
10⁸
Device power <n>

Fig. 7. Microwave resonator characterization of sample A-C. (a) Box plots showing the distribution of measured Q_i at low power ($\langle n_{ph} \rangle \approx 0.1$) for each specimen type. Each data point represents the median Q_i for one particular resonator measured. **(b)** Box plots showing the distribution of measured Q_i at high power ($\langle n_{ph} \rangle \approx 10^8$) for each specimen type. Each data point represents the median Q_i for one particular resonator measured. **(c)** Values of $F \times \delta_{tls}$ after fitting power-dependent loss to the TLS fit model. Each data point represents the median $F \times \delta_{tls}$ fit for one particular resonator. **(d)** Values of δ_{HP} (power-independent loss). Each data point represents the median δ_{HP} for one particular resonator. **(e)** Representative Q_i power spectra for three selected resonators, showing the variation between different measurement sweeps.

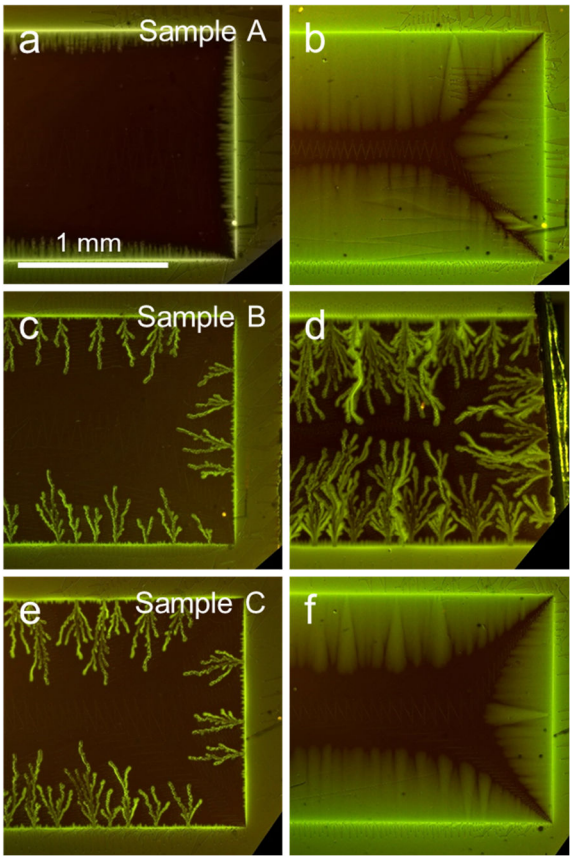

Fig. 8. Magnetic flux penetration in sample A-C. Intensity is proportional to the magnetic induction on the surface in **(a-b)** sample A and **(c-d)** sample B, and **(e-f)** sample C, as described in Methods. Each row shows results for the indicated samples at two temperatures, 4 K and 6 K. (**a,c,e)** Samples A-C were cooled to 4 K, and then a magnetic field of 40 Oe was applied. **(b,d,f)** Similar procedure at 6 K and with a magnetic field of 80 Oe. See the discussion in **Section 3.6** that correlates these results with the morphological and quality-factor observations.

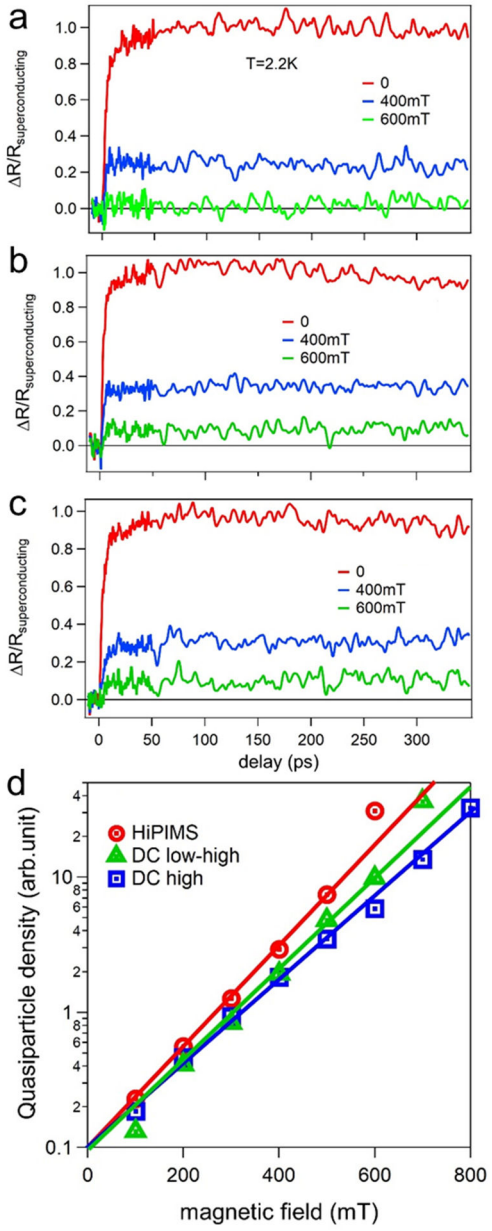

Fig. 9. Ultrafast spectroscopy probe of superfluid and quasi-particle dynamics in superconducting states of samples A, B, and C. (a) Normalized pump-induced reflectivity changes in the superconducting states, denoted as $\Delta R/R_{superconducting}$, of sample A, **(b)** sample B, and **(c)** sample C at 2.2K under different magnetic fields. The $\Delta R/R_{superconducting}$ signals are proportional to the pump-induced change of superfluid density. **(d)** Thermalized quasi-particle density is extracted from the superconducting states vs magnetic field of sample A (red circles), sample B (green triangles), and sample C (blue rectangles). These lines function as reference guides for the rate of generation of quasiparticles induced by the magnetic field.

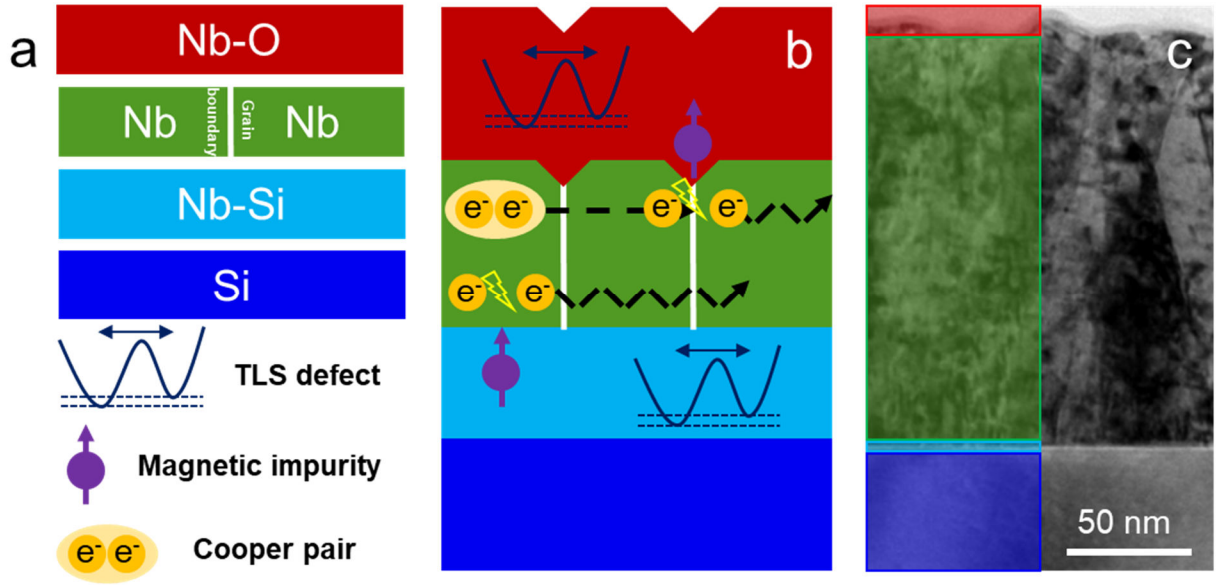

Fig. 10. Schematic illustrations of various microstructural features of Nb/Si-based resonators contributing to different loss mechanisms. (a) Boxes: Nb-O interface (red), Nb thin film (green), Nb-Si interface (light blue), and Si substrate (blue). Other drawings: TLS defect, magnetic impurity, and Cooper pair. **(b)** Schematic illustration identifying individual regions as specific loss sources, including Cooper pair breaking which leads to inductive loss. **(c)** Correlation of schematics to the cross-sectional TEM micrograph. Detailed description is in **Section 3.8**.

Table. 1. Table of average grain size, RRR, Q_i, and loss of sample A-C.

Sample	A (HiPIMS)	B (Low-High DC)	C (High DC)
Average grain size (nm)	44.0 ± 13.8	68.8 ± 25.2	65.3 ± 21.6
RRR=R(290 K)/R(10 K)	4.55 ± 0.1	6.66 ± 0.1	6.53 ± 0.1
Low power Q_i ($\times 10^5$)	1.70 ± 1.16	3.11 ± 2.26	9.83 ± 3.18
High power Q_i ($\times 10^5$)	3.01 ± 1.88	5.16 ± 3.60	17.0 ± 3.98
TLS loss ($\times 10^{-6}$)	1.93 ± 0.85	1.00 ± 0.76	1.32 ± 0.94
Power independent loss ($\times 10^{-6}$)	4.49 ± 2.07	2.82 ± 1.50	0.63 ± 1.62

Table. 2. Summary of interface/defects and potential source of losses

Microstructural feature	TLS origin	Non-TLS origin
Surface Nb oxides	Amorphous NbO_x (especially, Nb_2O_5)	Magnetic impurities in non-stoichiometric Nb_2O_5 and suboxides
Nb-Si interface (L1)	Amorphous Nb_xSi_y	Magnetism in Nb silicide (when thicker)
Grain boundary in Nb	Impurities diffusion into grain boundaries and triple junctions	Chemical and structural defects

References

[1] R.P. Feynman, Simulating physics with computers, International Journal of Theoretical Physics 21 (1982) 467–488. https://doi.org/10.1007/BF02650179.

[2] M. Vogel, Quantum Computation and Quantum Information, by M.A. Nielsen and I.L. Chuang, 2011. https://doi.org/10.1080/00107514.2011.587535.

[3] S. McArdle, S. Endo, A. Aspuru-Guzik, S.C. Benjamin, X. Yuan, Quantum computational chemistry, Rev Mod Phys 92 (2020) 15003. https://doi.org/10.1103/RevModPhys.92.015003.

[4] P.W. Shor, Polynomial-time algorithms for prime factorization and discrete logarithms on a quantum computer, SIAM Journal on Computing 26 (1997) 1484–1509. https://doi.org/10.1137/S0097539795293172.

[5] F. Arute, K. Arya, R. Babbush, D. Bacon, J.C. Bardin, R. Barends, R. Biswas, S. Boixo, F.G.S.L. Brandao, D.A. Buell, B. Burkett, Y. Chen, Z. Chen, B. Chiaro, R. Collins, W. Courtney, A. Dunsworth, E. Farhi, B. Foxen, A. Fowler, C. Gidney, M. Giustina, R. Graff, K. Guerin, S. Habegger, M.P. Harrigan, M.J. Hartmann, A. Ho, M. Hoffmann, T. Huang, T.S. Humble, S. V. Isakov, E. Jeffrey, Z. Jiang, D. Kafri, K. Kechedzhi, J. Kelly, P. V. Klimov, S. Knysh, A. Korotkov, F. Kostritsa, D. Landhuis, M. Lindmark, E. Lucero, D. Lyakh, S. Mandrà, J.R. McClean, M. McEwen, A. Megrant, X. Mi, K. Michielsen, M. Mohseni, J. Mutus, O. Naaman, M. Neeley, C. Neill, M.Y. Niu, E. Ostby, A. Petukhov, J.C. Platt, C. Quintana, E.G. Rieffel, P. Roushan, N.C. Rubin, D. Sank, K.J. Satzinger, V. Smelyanskiy, K.J. Sung, M.D. Trevithick, A. Vainsencher, B. Villalonga, T. White, Z.J. Yao, P. Yeh, A. Zalcman, H. Neven, J.M. Martinis, Quantum supremacy using a programmable superconducting processor, Nature 574 (2019) 505–510. https://doi.org/10.1038/s41586-019-1666-5.

[6] M.S. Alam, S. Belomestnykh, N. Bornman, G. Cancelo, Y.-C. Chao, M. Checchin, V.S. Dinh, A. Grassellino, E.J. Gustafson, R. Harnik, C.R.H. McRae, Z. Huang, K. Kapoor, T. Kim, J.B. Kowalkowski, M.J. Kramer, Y. Krasnikova, P. Kumar, D.M. Kurkcuoglu, H. Lamm, A.L. Lyon, D. Milathianaki, A. Murthy, J. Mutus, I. Nekrashevich, J. Oh, A.B. Özgüler, G.N. Perdue, M. Reagor, A. Romanenko, J.A. Sauls, L. Stefanazzi, D. Venturelli, C. Wang, X. You, D.M.T. van Zanten, L. Zhou, S. Zhu, S. Zorzetti, Quantum computing hardware for HEP algorithms and sensing, ArXiv (2022) 1–23. https://doi.org/10.48550/arXiv.2204.08605.

[7] M.H. Devoret, R.J. Schoelkopf, Superconducting circuits for quantum information: An outlook, Science (1979) 339 (2013) 1169–1174. https://doi.org/10.1126/science.1231930.

[8] J.M. Martinis, M.H. Devoret, J. Clarke, Quantum Josephson junction circuits and the dawn of artificial atoms, Nat Phys 16 (2020) 234–237. https://doi.org/10.1038/s41567-020-0829-5.

[9] N.P. de Leon, K.M. Itoh, D. Kim, K.K. Mehta, T.E. Northup, H. Paik, B.S. Palmer, N. Samarth, S. Sangtawesin, D.W. Steuerman, Materials challenges and opportunities for quantum computing hardware, Science (1979) 372 (2021). https://doi.org/10.1126/science.abb2823.

[10] Y. Nakamura, Y. ~A. Pashkin, J. ~S. Tsai, Coherent control of macroscopic quantum states in a single-Cooper-pair box, Nature 398 (1999) 786–788.

[11] T.P. Orlando, J.E. Mooij, L. Tian, C.H. Van Der Wal, L.S. Levitov, S. Lloyd, J.J. Mazo, Superconducting persistent-current qubit, Phys Rev B Condens Matter Mater Phys 60 (1999) 15398–15413. https://doi.org/10.1103/PhysRevB.60.15398.

[12] J. Koch, T.M. Yu, J. Gambetta, A.A. Houck, D.I. Schuster, J. Majer, A. Blais, M.H. Devoret, S.M. Girvin, R.J. Schoelkopf, Charge-insensitive qubit design derived from the Cooper pair box, Phys Rev A 76 (2007) 1–19. https://doi.org/10.1103/PhysRevA.76.042319.

[13] J.A. Schreier, A.A. Houck, J. Koch, D.I. Schuster, B.R. Johnson, J.M. Chow, J.M. Gambetta, J. Majer, L. Frunzio, M.H. Devoret, S.M. Girvin, R.J. Schoelkopf, Suppressing charge noise decoherence in superconducting charge qubits, Phys Rev B Condens Matter Mater Phys 77 (2008) 2–5. https://doi.org/10.1103/PhysRevB.77.180502.

[14] H. Paik, D.I. Schuster, L.S. Bishop, G. Kirchmair, G. Catelani, A.P. Sears, B.R. Johnson, M.J. Reagor, L. Frunzio, L.I. Glazman, S.M. Girvin, M.H. Devoret, R.J. Schoelkopf, Observation of high coherence in Josephson junction qubits measured in a three-dimensional circuit QED architecture, Phys Rev Lett 107 (2011) 1–5. https://doi.org/10.1103/PhysRevLett.107.240501.

[15] E. Sheridan, T.F. Harrelson, E. Sivonxay, K.A. Persson, M.V.P. Altoé, I. Siddiqi, D.F. Ogletree, D.I. Santiago, S.M. Griffin, Microscopic Theory of Magnetic Disorder-Induced Decoherence in Superconducting Nb Films, ArXiv (2021) 1–10. http://arxiv.org/abs/2111.11684.

[16] A. Nersisyan, E.A. Sete, S. Stanwyck, A. Bestwick, M. Reagor, S. Poletto, N. Alidoust, R. Manenti, R. Renzas, C.V. Bui, K. Vu, T. Whyland, Y. Mohan, Manufacturing low dissipation superconducting quantum processors, Technical Digest - International Electron Devices Meeting, IEDM 2019-Decem (2019). https://doi.org/10.1109/IEDM19573.2019.8993458.

[17] R. McDermott, Materials origins of decoherence in superconducting qubits, IEEE Transactions on Applied Superconductivity 19 (2009) 2–13. https://doi.org/10.1109/TASC.2008.2012255.

[18] C.R.H. McRae, H. Wang, J. Gao, M.R. Vissers, T. Brecht, A. Dunsworth, D.P. Pappas, J. Mutus, Materials loss measurements using superconducting microwave resonators, Review of Scientific Instruments 91 (2020) 091101. https://doi.org/10.1063/5.0017378.

[19] J. Lisenfeld, G.J. Grabovskij, C. Müller, J.H. Cole, G. Weiss, A. V. Ustinov, Observation of directly interacting coherent two-level systems in an amorphous material, Nat Commun 6 (2015) 1–6. https://doi.org/10.1038/ncomms7182.

[20] C. Müller, J.H. Cole, J. Lisenfeld, Towards understanding two-level-systems in amorphous solids: Insights from quantum circuits, Reports on Progress in Physics 82 (2019) 124501. https://doi.org/10.1088/1361-6633/ab3a7e.

[21] W.A. Phillips, Two-level states in glasses, Reports on Progress in Physics 50 (1987) 1657–1708. https://doi.org/10.1088/0034-4885/50/12/003.

[22] P. Kumar, S. Sendelbach, M.A. Beck, J.W. Freeland, Z. Wang, H. Wang, C.C. Yu, R.Q. Wu, D.P. Pappas, R. McDermott, Origin and Suppression of $1/f$ Magnetic Flux Noise, (2016). https://doi.org/10.1103/PhysRevApplied.6.041001.

[23] E. V. Bezuglyi, A.S. Vasenko, E.N. Bratus, V.S. Shumeiko, G. Wendin, Subgap current in superconducting tunnel junctions with diffusive electrodes, Phys Rev B Condens Matter Mater Phys 73 (2006) 1–4. https://doi.org/10.1103/PhysRevB.73.220506.

[24] M.V.P. Altoé, A. Banerjee, C. Berk, A. Hajr, A. Schwartzberg, C. Song, M. Alghadeer, S. Aloni, M.J. Elowson, J.M. Kreikebaum, E.K. Wong, S.M. Griffin, S. Rao, A. Weber-Bargioni, A.M. Minor, D.I. Santiago, S. Cabrini, I. Siddiqi, D.F. Ogletree, Localization and Mitigation of Loss in Niobium Superconducting Circuits, PRX Quantum 3 (2022) 020312. https://doi.org/10.1103/PRXQuantum.3.020312.

[25] D.P. Pappas, M.R. Vissers, D.S. Wisbey, J.S. Kline, J. Gao, Two level system loss in superconducting microwave resonators, IEEE Transactions on Applied Superconductivity 21 (2011) 871–874. https://doi.org/10.1109/TASC.2010.2097578.

[26] P. Foshat, P. Baity, S. Danilin, V. Seferai, S. Poorgholam-Khanjari, H. Feng, O.A. Mukhanov, M. Hutchings, R.H. Hadfield, M. Imran, M. Weides, K. Delfanazari, Characterizing Niobium Nitride Superconducting Microwave Coplanar Waveguide Resonator Array for Circuit Quantum Electrodynamics in Extreme Conditions, ArXiv (2023). https://doi.org/https://doi.org/10.48550/arXiv.2306.02356.

[27] C.E. Murray, Material matters in superconducting qubits, Materials Science and Engineering R: Reports 146 (2021). https://doi.org/10.1016/j.mser.2021.100646.

[28] A. Blais, R.S. Huang, A. Wallraff, S.M. Girvin, R.J. Schoelkopf, Cavity quantum electrodynamics for superconducting electrical circuits: An architecture for quantum computation, Phys Rev A (Coll Park) 69 (2004) 1–14. https://doi.org/10.1103/PhysRevA.69.062320.

[29] W.D. Oliver, P.B. Welander, Materials in superconducting quantum bits, MRS Bull 38 (2013) 816–825. https://doi.org/10.1557/mrs.2013.229.

[30] A. Blais, A.L. Grimsmo, S.M. Girvin, A. Wallraff, Circuit quantum electrodynamics, Rev Mod Phys 93 (2021) 025005. https://doi.org/10.1103/RevModPhys.93.025005.

[31] A. Wallraff, D.I. Schuster, A. Blais, L. Frunzio, R.S. Huang, J. Majer, S. Kumar, S.M. Girvin, R.J. Schoelkopf, Strong coupling of a single photon to a superconducting qubit using circuit quantum electrodynamics, Nature 431 (2004) 162–167. https://doi.org/10.1038/nature02851.

[32] T.F. Harrelson, E. Sheridan, E. Kennedy, J. Vinson, A.T. N'Diaye, M.V.P. Altoé, A. Schwartzberg, I. Siddiqi, D.F. Ogletree, M.C. Scott, S.M. Griffin, Elucidating the local atomic and electronic structure of amorphous oxidized superconducting niobium films, Appl Phys Lett 119 (2021) 244004. https://doi.org/10.1063/5.0069549.

[33] A.A. Murthy, P. Masih Das, S.M. Ribet, C. Kopas, J. Lee, M.J. Reagor, L. Zhou, M.J. Kramer, M.C. Hersam, M. Checchin, A. Grassellino, R. dos Reis, V.P. Dravid, A. Romanenko, Developing a Chemical and Structural Understanding of the Surface Oxide in a Niobium Superconducting Qubit, ACS Nano (2022). https://doi.org/10.1021/acsnano.2c07913.

[34] J. Oh, X. Fang, T. Kim, M. Lynn, M. Kramer, J.A. Sauls, A. Romanenko, S. Posen, A. Grassellino, J. Cameron, M. Field, J. Marshall, H. Cansizoglu, K. Yadavalli, J.Y. Mutus, M. Reagor, L. Zhou, In-situ

Transmission Electron Microscopy Investigation on Surface Oxides Thermal Stability of Niobium, Appl Surf Sci (2023) 157297. https://doi.org/10.1016/j.apsusc.2023.157297.

[35] A.A. Murthy, J. Lee, C. Kopas, M.J. Reagor, A.P. Mcfadden, D.P. Pappas, M. Checchin, A. Grassellino, A. Romanenko, TOF-SIMS analysis of decoherence sources in superconducting qubits, Appl Phys Lett 120 (2022). https://doi.org/10.1063/5.0079321.

[36] J. Verjauw, A. Potočnik, M. Mongillo, R. Acharya, F. Mohiyaddin, G. Simion, A. Pacco, Ts. Ivanov, D. Wan, A. Vanleenhove, L. Souriau, J. Jussot, A. Thiam, J. Swerts, X. Piao, S. Couet, M. Heyns, B. Govoreanu, I. Radu, Investigation of microwave loss induced by oxide regrowth in high-Q Nb resonators, Phys Rev Appl 014018 (2021) 1–18. https://doi.org/10.1103/PhysRevApplied.16.014018.

[37] A. Premkumar, C. Weiland, S. Hwang, B. Jäck, A.P.M. Place, I. Waluyo, A. Hunt, V. Bisogni, J. Pelliciari, A. Barbour, M.S. Miller, P. Russo, F. Camino, K. Kisslinger, X. Tong, M.S. Hybertsen, A.A. Houck, I. Jarrige, Microscopic relaxation channels in materials for superconducting qubits, Commun Mater 2 (2021) 72. https://doi.org/10.1038/s43246-021-00174-7.

[38] P. Dutta, P.M. Horn, Low-frequency fluctuations in solids: 1/f noise, Rev Mod Phys 53 (1981) 497–516. https://doi.org/10.1103/RevModPhys.53.497.

[39] A. Shnirman, G. Schön, I. Martin, Y. Makhlin, Low- And high-frequency noise from coherent two-level systems, Phys Rev Lett 94 (2005) 1–4. https://doi.org/10.1103/PhysRevLett.94.127002.

[40] J. Burnett, L. Faoro, I. Wisby, V.L. Gurtovoi, A. V. Chernykh, G.M. Mikhailov, V.A. Tulin, R. Shaikhaidarov, V. Antonov, P.J. Meeson, A.Y. Tzalenchuk, T. Lindström, Evidence for interacting two-level systems from the 1/f noise of a superconducting resonator, Nat Commun 5 (2014) 1–6. https://doi.org/10.1038/ncomms5119.

[41] W. Woods, G. Calusine, A. Melville, A. Sevi, E. Golden, D.K. Kim, D. Rosenberg, J.L. Yoder, W.D. Oliver, Determining Interface Dielectric Losses in Superconducting Coplanar-Waveguide Resonators, Phys Rev Appl 12 (2019) 1. https://doi.org/10.1103/PhysRevApplied.12.014012.

[42] A. Romanenko, D.I. Schuster, Understanding Quality Factor Degradation in Superconducting Niobium Cavities at Low Microwave Field Amplitudes, Phys Rev Lett 119 (2017) 1–6. https://doi.org/10.1103/PhysRevLett.119.264801.

[43] X. Fang, J.-S. Oh, M. Kramer, A. Romanenko, A. Grassellino, J. Zasadzinski, L. Zhou, Understanding the Mechanism of the Performance Improvement in Nitrogen-doped Niobium Superconducting Radio Frequency Cavity, Mater Res Lett 11 (2022) 108–116. https://doi.org/10.1080/21663831.2022.2126737.

[44] A. Romanenko, R. Pilipenko, S. Zorzetti, D. Frolov, M. Awida, S. Belomestnykh, S. Posen, A. Grassellino, Three-Dimensional Superconducting Resonators at T<20 mK with Photon Lifetimes up to τ=2 s, Phys Rev Appl 13 (2020) 1. https://doi.org/10.1103/PhysRevApplied.13.034032.

[45] M. Bal, A.A. Murthy, S. Zhu, F. Crisa, X. You, Z. Huang, T. Roy, J. Lee, D. van Zanten, R. Pilipenko, I. Nekrashevich, A. Lunin, D. Bafia, Y. Krasnikova, C.J. Kopas, E.O. Lachman, D. Miller, J.Y. Mutus, M.J. Reagor, H. Cansizoglu, J. Marshall, D.P. Pappas, K. Vu, K. Yadavalli, J.-S. Oh, L. Zhou, M.J.

Kramer, F.Q. Lecocq, D.P. Goronzy, C.G. Torres-Castanedo, G. Pritchard, V.P. Dravid, J.M. Rondinelli, M.J. Bedzyk, M.C. Hersam, J. Zasadzinski, J. Koch, J.A. Sauls, A. Romanenko, A. Grassellino, Systematic Improvements in Transmon Qubit Coherence Enabled by Niobium Surface Encapsulation, Npj Quantum Inf 10 (2024) 43. https://doi.org/10.1038/s41534-024-00840-x.

[46] M. Delheusy, A. Stierle, N. Kasper, R.P. Kurta, A. Vlad, H. Dosch, C. Antoine, A. Resta, E. Lundgren, J. Andersen, X-ray investigation of subsurface interstitial oxygen at Nb/oxide interfaces, Appl Phys Lett 92 (2008) 8–11. https://doi.org/10.1063/1.2889474.

[47] D.P. Lozano, M. Mongillo, X. Piao, S. Couet, D. Wan, Y. Canvel, A.M. Vadiraj, Ts. Ivanov, J. Verjauw, R. Acharya, J. Van Damme, F.A. Mohiyaddin, J. Jussot, P.P. Gowda, A. Pacco, B. Raes, J. Van de Vondel, I.P. Radu, B. Govoreanu, J. Swerts, A. Potočnik, K. De Greve, Manufacturing high-Q superconducting {\alpha}-tantalum resonators on silicon wafers, (2022).

[48] X. Lu, D.P. Goronzy, C.G. Torres-Castanedo, P. Masih Das, M. Kazemzadeh-Atoufi, A. McFadden, C.R.H. McRae, P.W. Voorhees, V.P. Dravid, M.J. Bedzyk, M.C. Hersam, J.M. Rondinelli, Stability, metallicity, and magnetism in niobium silicide nanofilms, Phys Rev Mater 6 (2022) 1–11. https://doi.org/10.1103/PhysRevMaterials.6.064402.

[49] C. Kopas, M.K. Murthy, C. Gregory, B.I. Mercado, D.R. Queen, B. Wagner, N. Newman, Characterization of the Chemical and Electrical Properties of defects at the Niobium-Silicon Interface, ArXiv (2020).

[50] J.-S. Oh, X. Fang, T.-H. Kim, M. Lynn, M. Kramer, M. Zarea, J. Sauls, A. Romanenko, S. Posen, A. Grassellino, C.J. Kopas, M. Field, J. Marshall, H. Cansizoglu, J.Y. Mutus, M. Reagor, L. Zhou, Multi-Modal Electron Microscopy Investigation on Decoherence Sources and Their Stability in Nb Based Superconducting Qubit, ArXiv (2022) 1–27. https://doi.org/10.2139/ssrn.4128730.

[51] C. Jooss, J. Albrecht, H. Kuhn, S. Leonhardt, H. Kronmuller, Magneto-Optical Studies of Current Distributions in High T Superconductors, Reports on Progress in Physics 65 (2002) 651–788.

[52] A. Anders, J. Andersson, A. Ehiasarian, High power impulse magnetron sputtering: Current-voltage-time characteristics indicate the onset of sustained self-sputtering, J Appl Phys 102 (2007). https://doi.org/10.1063/1.2817812.

[53] S. Wilde, R. Valizadeh, O.B. Malyshev, G.B.G. Stenning, T. Sian, B. Chesca, Dc magnetometry of niobium thin film superconductors deposited using high power impulse magnetron sputtering, Physical Review Accelerators and Beams 21 (2018) 73101. https://doi.org/10.1103/PhysRevAccelBeams.21.073101.

[54] A.M. Engwall, S.J. Shin, J. Bae, Y.M. Wang, Enhanced properties of tungsten films by high-power impulse magnetron sputtering, Surf Coat Technol 363 (2019) 191–197. https://doi.org/10.1016/j.surfcoat.2019.02.055.

[55] D. Bach, R. Schneider, D. Gerthsen, J. Verbeeck, W. Sigle, EELS of Niobium and Stoichiometric Niobium-Oxide Phases—Part I: Plasmon and Near-Edges Fine Structure, Microscopy and Microanalysis 15 (2009) 505–523. https://doi.org/10.1017/S143192760999105X.

[56] L.D. Alegria, D.M. Tennant, K.R. Chaves, J.R.I. Lee, S.R. O'Kelley, Y.J. Rosen, J.L. DuBois, Two-level systems in nucleated and non-nucleated epitaxial alpha-tantalum films, Appl Phys Lett 123 (2023). https://doi.org/10.1063/5.0157654.

[57] S. Nik, P. Krantz, L. Zeng, T. Greibe, H. Pettersson, S. Gustafsson, P. Delsing, E. Olsson, Correlation between Al grain size, grain boundary grooves and local variations in oxide barrier thickness of Al/AlOx/Al tunnel junctions by transmission electron microscopy, Springerplus 5 (2016). https://doi.org/10.1186/s40064-016-2418-8.

[58] L. Tang, D.E. Laughlin, Electron Diffraction Patterns of Fibrous and Lamellar Textured Polycrystalline Thin Films. I. Theory, J Appl Crystallogr 29 PART 4 (1996) 411–418. https://doi.org/10.1107/s0021889896000404.

[59] L. Tang, Y.C. Feng, L.L. Lee, D.E. Laughlin, Electron Diffraction Patterns of Fibrous and Lamellar Textured Polycrystalline Thin Films. II. Applications, J Appl Crystallogr 29 PART 4 (1996) 419–426. https://doi.org/10.1107/s0021889896000416.

[60] C. V. Thompson, R. Carel, Texture development in polycrystalline thin films, Materials Science and Engineering B 32 (1995) 211–219. https://doi.org/10.1016/0921-5107(95)03011-5.

[61] J. Halbritter, On the oxidation and on the superconductivity of niobium, Applied Physics A Solids and Surfaces 43 (1987) 1–28. https://doi.org/10.1007/BF00615201.

[62] R.M. Waterstrat, F. Haenssler, J. Müller, Nb-Si A15 compounds produced by liquid quenching, J Appl Phys 50 (1979) 4763–4766. https://doi.org/10.1063/1.326535.

[63] T. Masumoto, A. Inoue, S. Sakai, H. Kimura, A. Hoshi, SUPERCONDUCTIVITY OF DUCTILE Nb-BASED AMORPHOUS ALLOYS., Transactions of the Japan Institute of Metals 21 (1980) 115–122. https://doi.org/10.2320/matertrans1960.21.115.

[64] E.W. Collings, C.C. Koch, Undercooled alloy phases : proceedings of the 1986 Hume-Rothery Memorial Symposium which was organized by the TMS Committee on Alloy Phases, and was held in New Orleans, Louisiana, March 2-6, 1986 at the 115th annual meeting of TMS-AIME / edited by E.W. Collings, C.C. Koch., 1987.

[65] H. Iwasaki, W.K. Wang, N. Toyota, T. Fukase, H. Fujimori, Y. Akahama, S. Endo, A15Nb3Si produced by high-pressure annealing of amorphous sputter deposits, Solid State Commun 42 (1982) 381–384. https://doi.org/10.1016/0038-1098(82)90158-2.

[66] K. Georgarakis, Y. Li, M. Aljerf, D. Dudina, A. LeMoulec, A.R. Yavari, G. Vaughan, A. Inoue, Glass formation in the Nb–Si binary system, J Alloys Compd 504 (2010) S14–S17. https://doi.org/10.1016/j.jallcom.2010.03.034.

[67] R. Busch, Thermophysical properties of bulk metallic glass-forming liquids, Jom 52 (2000) 39–42. https://doi.org/10.1007/s11837-000-0160-7.

[68] T.B. Massalski, H. Okamoto, Binary alloy phase diagrams / editor-in-chief, Thaddeus B. Massalski ; editors, Hiroaki Okamoto, P.R. Subramanian, Linda Kacprzak., 2nd ed.., 1990.

[69] B. Bonin, H. Safa, Power dissipation at high fields in granular RF superconductivity, Supercond Sci Technol 4 (1991) 257–261. https://doi.org/10.1088/0953-2048/4/6/008.

[70] T. Proslier, M. Kharitonov, M. Pellin, J. Zasadzinski, G. Ciovati, Evidence of surface paramagnetism in niobium and consequences for the superconducting cavity surface impedance, IEEE Transactions on Applied Superconductivity 21 (2011) 2619–2622. https://doi.org/10.1109/TASC.2011.2107491.

[71] K.R. Joshi, S. Ghimire, M.A. Tanatar, A. Datta, J.-S. Oh, L. Zhou, C.J. Kopas, J. Marshall, J.Y. Mutus, J. Slaughter, M.J. Kramer, J.A. Sauls, R. Prozorov, Quasiparticle spectroscopy, transport, and magnetic properties of Nb films used in superconducting transmon qubits, Phys Rev Appl 20 (2023) 024031. https://doi.org/10.1103/PhysRevApplied.20.024031.

[72] G. Berti, C.G. Torres-Castanedo, D.P. Goronzy, M.J. Bedzyk, M.C. Hersam, C. Kopas, J. Marshall, M. Iavarone, Scanning tunneling microscopy and spectroscopy characterization of Nb films for quantum applications, Appl Phys Lett 122 (2023). https://doi.org/10.1063/5.0145090.

[73] X. Yang, L. Luo, M. Mootz, A. Patz, S.L. Bud'Ko, P.C. Canfield, I.E. Perakis, J. Wang, Nonequilibrium Pair Breaking in Ba (Fe1-xCox)2As2 Superconductors: Evidence for Formation of a Photoinduced Excitonic State, Phys Rev Lett 121 (2018) 267001. https://doi.org/10.1103/PhysRevLett.121.267001.

[74] A. Rothwarf, B.N. Taylor, Measurement of recombination lifetimes in superconductors, Phys Rev Lett 19 (1967) 27–30. https://doi.org/10.1103/PhysRevLett.19.27.

[75] V. V. Kabanov, J. Demsar, D. Mihailovic, Kinetics of a superconductor excited with a femtosecond optical pulse, Phys Rev Lett 95 (2005) 147002. https://doi.org/10.1103/PhysRevLett.95.147002.

[76] X. Yang, X. Zhao, C. Vaswani, C. Sundahl, B. Song, Y. Yao, D. Cheng, Z. Liu, P.P. Orth, M. Mootz, J.H. Kang, I.E. Perakis, C.Z. Wang, K.M. Ho, C.B. Eom, J. Wang, Ultrafast nonthermal terahertz electrodynamics and possible quantum energy transfer in the Nb3Sn superconductor, Phys Rev B 99 (2019) 1–8. https://doi.org/10.1103/PhysRevB.99.094504.

[77] B. Cheng, D. Cheng, K. Lee, L. Luo, Z. Chen, Y. Lee, B.Y. Wang, M. Mootz, I.E. Perakis, Z.X. Shen, H.Y. Hwang, J. Wang, Evidence for d-wave superconductivity of infinite-layer nickelates from low-energy electrodynamics, Nat Mater (2024). https://doi.org/10.1038/s41563-023-01766-z.

[78] S.E. de Graaf, L. Faoro, L.B. Ioffe, S. Mahashabde, J.J. Burnett, T. Lindström, S.E. Kubatkin, A. V. Danilov, A.Y. Tzalenchuk, Two-level systems in superconducting quantum devices due to trapped quasiparticles, Sci Adv 6 (2020) 1–9. https://doi.org/10.1126/SCIADV.ABC5055.

[79] M. Kharitonov, T. Proslier, A. Glatz, M.J. Pellin, Surface impedance of superconductors with magnetic impurities, Phys Rev B Condens Matter Mater Phys 86 (2012) 1–8. https://doi.org/10.1103/PhysRevB.86.024514.